# Supporting Information

## SI Theory

**A. Definition of the Complex Gaussian Distribution.** We define $\varepsilon = \varepsilon_r + i\varepsilon_i$, where the real and imaginary components are independent, zero mean Gaussian random variables with variance $\sigma_\varepsilon^2/2$. The one-dimensional circularly symmetric complex Gaussian distribution is [29]

$$p(\varepsilon) = (\pi\sigma_\varepsilon^2)^{-1} \exp\left(-\frac{\varepsilon\varepsilon^*}{\sigma_\varepsilon^2}\right) \triangleq \mathcal{CN}(\varepsilon; 0, \sigma_\varepsilon^2), \qquad [S1]$$

where $\varepsilon^* = \varepsilon_r - i\varepsilon_i$ is the complex conjugate of $\varepsilon$.

**B. Derivation of the Complex Kalman Filter Algorithm.** We derive the parallel, one-dimensional complex Kalman filter algorithms by following the standard *maximum a posteriori* derivation of the Kalman filter algorithm [23]. To define the recursive estimator of $\Delta Z_k^{(m)}$, we use Bayes' rule and express the posterior density of $\Delta Z_k^{(m)}$ given all of the data, $Y_{1:k}^{(m),F}$, up through interval $k$ as

$$p(\Delta Z_k^{(m)}|Y_{1:k}^{(m),F}) = \frac{p(\Delta Z_k^{(m)}|Y_{1:k-1}^{(m),F})p(Y_k^{(m),F}|\Delta Z_k)}{p(Y_k^{(m),F}|Y_{1:k-1}^{(m),F})}, \qquad [S2]$$

where the first term on the right side of Eq. S2 is the one-step prediction density defined by the Chapman-Kolmogorov equation as

$$p(\Delta Z_k^{(m)}|Y_{1:k-1}^{(m),F}) = \int p(\Delta Z_{k-1}^{(m)}|Y_{1:k-1}^{(m),F})p(\Delta Z_k^{(m)}|\Delta Z_{k-1}^{(m)})d\Delta Z_{k-1}^{(m)}. \qquad [S3]$$

The $\Delta Z_k^{(m)}(\omega_j)$ are independent for $j = 1, \ldots, J$ and for each $j$, $p(\Delta Z_k^{(m)}(\omega_j)|Y_{1:k-1,j}^{(m),F})$ is a one-dimensional circularly symmetric complex Gaussian distribution. Hence, given the recursion up through interval $k-1$ and the state model (Eq. 3), the one-step prediction density has the form

$$p(\Delta Z_k^{(m)}|Y_{1:k-1}^{(m),F}) = \prod_{j=1}^{J} \mathcal{CN}(\Delta Z_k^{(m)}(\omega_j); \Delta Z_{k|k-1}^{(m)}(\omega_j), \sigma_{k|k-1,j}^{2,(m)}), \qquad [S4]$$

where

$$\Delta Z_{k|k-1}^{(m)}(\omega_j) \triangleq E(\Delta Z_k^{(m)}(\omega_j)|Y_{1:k-1,j}^{(m),F}) = \Delta Z_{k-1|k-1}^{(m)}(\omega_j) \qquad [S5]$$

$$\sigma_{k|k-1,j}^{2,(m)} \triangleq E(||\Delta Z_k^{(m)}(\omega_j) - \Delta Z_{k|k-1}^{(m)}(\omega_j)||^2|Y_{1:k-1,j}^{(m),F}) = \sigma_{k-1|k-1,j}^{2,(m)} + \sigma_{v,j}^{2,(m)} \qquad [S6]$$

Moreover, the $Y_{k,j}^{(m),F}$ are also independent for $j = 1, \ldots, J$ and for each $j$, $p(Y_{k,j}^{(m),F}|\Delta Z_k^{(m)}(\omega_j))$ is a one-dimensional circularly symmetric complex Gaussian distribution that is defined by Eq. 5. Hence, the observation model at interval $k$ is

$$p(Y_k^{(m),F}|\Delta Z_k^{(m)}) = \prod_{j=1}^{J} \mathcal{CN}(Y_{k,j}^{(m),F}; \Delta Z_k^{(m)}(\omega_j), \sigma_\varepsilon^{2,(m)}). \qquad [S7]$$

The posterior density at interval $k$ is

$$p(\Delta Z_k^{(m)}|Y_{1:k}^{(m),F}) \propto p(\Delta Z_k^{(m)}|Y_{1:k-1}^{(m),F})p(Y_k^{(m),F}|\Delta Z_k^{(m)}), \qquad [S8]$$

and the log posterior density at interval $k$ is

$$\log p(\Delta Z_k^{(m)}|Y_{1:k}^{(m),F}) = -\sum_{j=1}^{J} \frac{||Y_{k,j}^{(m),F} - \Delta Z_k^{(m)}(\omega_j)||^2}{\sigma_\varepsilon^{2,(m)}} - \sum_{j=1}^{J} \frac{||\Delta Z_k^{(m)}(\omega_j) - \Delta Z_{k|k-1}^{(m)}(\omega_j))||^2}{\sigma_{k|k-1,j}^{2,(m)}}. \qquad [S9]$$

The $J$ pairs of one-step prediction densities and observation models are independent. Therefore, differentiating Eq. S9 with respect to $\Delta Z_k^{(m)*}(\omega_j)$ gives

$$\frac{\partial \log p(\Delta Z_k^{(m)}|Y_{1:k}^{(m),F})}{\partial \Delta Z_k^{(m)*}(\omega_j)} = \frac{\Delta Z_k^{(m)}(\omega_j) - \Delta Z_{k|k-1}^{(m)}(\omega_j)}{\sigma_{k|k-1,j}^{2,(m)}} - \frac{Y_{k,j}^{(m),F} - \Delta Z_k^{(m)}(\omega_j)}{\sigma_\varepsilon^{2,(m)}}, \qquad [S10]$$

for $j = 1, \ldots, J$. Setting Eq. S10 equal to zero yields the recursion of estimate $\Delta Z_{k|k}^{(m)}(\omega_j)$

$$\Delta Z_{k|k}^{(m)}(\omega_j) = \frac{\sigma_\varepsilon^{2,(m)}\Delta Z_{k|k-1}^{(m)}(\omega_j) + \sigma_{k|k-1,j}^{2,(m)}Y_{k,j}^{(m),F}}{\sigma_{k|k-1,j}^{2,(m)} + \sigma_\varepsilon^{2,(m)}}. \qquad [S11]$$

Setting $\sigma_{k|k,j}^{2,(m)}$ equal to the negative reciprocal of the second derivative of Eq. S9 gives

$$\sigma_{k|k,j}^{2(m)} = \left((\sigma_{k|k-1,j}^{2,(m)})^{-1} + (\sigma_\varepsilon^{2,(m)})^{-1}\right)^{-1}. \qquad [S12]$$

Eq. 7c (Eq. 7d) follows from Eq. S11 (Eq. S12) by applying the definition of the Kalman gain in Eq. 8. Eqs. S5, S6, S11, and S12 are the one-dimensional complex Kalman filter algorithm given in Eqs. 7a-7d.

**C. State-Space Multitaper Cross-Spectrogram Analysis.** By making standard assumptions regarding joint local stationarity between two or more time series, the SS-MT paradigm can be extended to compute SS-MT cross-spectrograms. We assume that we compute on interval $k$, the Fourier transforms of tapered data series $Y_k^{r,(m),F}$ and $Y_k^{s,(m),F}$ from recording locations $r$ and $s$, respectively. We compute the corresponding increment difference estimates from the two locations as $\Delta Z_{k|k}^{r,(m)}(\omega_j)$ and $\Delta Z_{k|k}^{s,(m)}(\omega_j)$, the $m$th SS-MT eigencross-spectrogram as

$$f_{k|k}^{SS-MT(r,s)(m)}(\omega_j) = \Delta Z_{k|k}^{r,(m)}(\omega_j) \cdot \Delta Z_{k|k}^{s,(m)}(\omega_j)^* \qquad [S13]$$

and the SS-MT cross-spectrogram estimate is

$$f_{k|k}^{SS-MT(r,s)}(\omega_j) = M^{-1}\sum_{m=1}^{M} f_{k|k}^{SS-MT(r,s)(m)}(\omega_j). \qquad [S14]$$

The corresponding SS-MT coherogram estimate is

$$C_{k|k}^{r,s}(\omega_j) = \frac{||f_{k|k}^{SS-MT(r,s)}(\omega_j)||}{(f_{k|k}^{SS-MT(r,r)}(\omega_j) \cdot f_{k|k}^{SS-MT(s,s)}(\omega_j))^{\frac{1}{2}}}. \qquad [S15]$$

**D. An EM Algorithm for Model Parameters and Initial State Estimation.** We use an EM algorithm to find the maximum-likelihood estimates of $\Theta = \{\sigma_\varepsilon^{2,(m)}, \sigma_{v,j}^{2,(m)}, \Delta Z_0^{(m)}\}$ [27]. It is computed by maximizing the expectation of completed data log-likelihood. The joint probability distribution of $\Delta Z_{1:K}^{(m)}(\omega_j)$ and $Y_{1:K,j}^{(m),F}$ at frequency $j$ can be written as:

$$\begin{aligned} L_j^{(m)} &= p(\Delta Z_0^{(m)}(\omega_j)|\sigma_{v,j}^{2,(m)}) \\ &\times \prod_{k=1}^{K} p(\Delta Z_k^{(m)}(\omega_j)|\Delta Z_{k-1}^{(m)}(\omega_j), \sigma_{v,j}^{2,(m)}) \\ &\times \prod_{k=1}^{K} p(Y_{k,j}^{(m),F}|\Delta Z_k^{(m)}(\omega_j), \sigma_\varepsilon^{2,(m)}), \end{aligned} \quad [S16]$$

where we assume that the probability density of the initial state is given by

$$p(\Delta Z_0^{(m)}(\omega_j)) = (\pi\sigma_{v,j}^{2,(m)})^{-1} \exp\left(-\frac{\|\Delta Z_0^{(m)}(\omega_j)\|^2}{\sigma_{v,j}^{2,(m)}}\right). \quad [S17]$$

***D.1. E-step.*** In iteration $l$ of the E-step, the algorithm computes the expectation of the complete data log-likelihood, given the observed data and the previous estimates of the parameters from iteration $l-1$. For simplicity, we omit the superscript $m$ for the tapered data series. Taking log and expectation to the likelihood yields

$$\begin{aligned} &E[\log L_j^{(l)} \mid Y_{1:K,j}^F, \Theta^{(l-1)}] \\ &= E\left[-\frac{\|\Delta Z_0^{(l)}(\omega_j)\|^2}{\sigma_{v,j}^{2,(l-1)}} - \frac{1}{\sigma_\varepsilon^{2,(l-1)}}\sum_{k=1}^{K}\|Y_{k,j}^{F,(l)} - \Delta Z_k^{(l)}(\omega_j)\|^2 \right. \\ &\quad - K\log(\pi\sigma_\varepsilon^{2,(l-1)}) - (K+1)\log(\pi\sigma_{v,j}^{2,(l-1)}) \\ &\quad \left. -\frac{1}{\sigma_{v,j}^{2,(l-1)}}\sum_{k=1}^{K}\|\Delta Z_k^{(l)}(\omega_j) - \Delta Z_{k-1}^{(l)}(\omega_j)\|^2 \mid Y_{1:K,j}^F\right]. \end{aligned} \quad [S18]$$

We need to compute three quantities to evaluate Eq. S18 for $k = 1, \cdots, K$. They are

$$\Delta Z_{k|K}^{(l)}(\omega_j) = E[\Delta Z_k(\omega_j) \mid Y_{1:K,j}^F, \Theta^{(l-1)}], \quad [S19]$$

$$W_{k|K,j}^{(l)} = E[\|\Delta Z_k(\omega_j)\|^2 \mid Y_{1:K,j}^F, \Theta^{(l-1)}], \quad [S20]$$

and

$$W_{k,k-1|K,j}^{(l)} = E[\Delta Z_k(\omega_j)\Delta Z_{k-1}^*(\omega_j) \mid Y_{1:K,j}^F, \Theta^{(l-1)}]. \quad [S21]$$

Following Smith and Brown [20], these 3 quantities can be efficiently computed using the Kalman filter (Eqs. 7 and 8), Kalman smoothing (Eq. 16) and covariance smoothing (Eq. 17) algorithms.

***D.2. M-step.*** To carry out the M-step we let $\tau_{v,j}^{(l)} = 1/\sigma_{v,j}^{2,(l)}$ and $\tau_\varepsilon^{(l)} = 1/\sigma_\varepsilon^{2,(l)}$ and assume that each has a gamma prior density defined as

$$p(\tau|\alpha,\beta) = \frac{\beta^\alpha}{\Gamma(\alpha)}(\tau)^{\alpha-1}\exp(-\beta\tau), \quad [S22]$$

for $\alpha > 1$ and $\beta > 0$. The expectation of log joint posterior density of $\tau_{v,j}^{(l)}$ and $\tau_\varepsilon^{(l)}$ is defined as

$$\begin{aligned} &E[\log p(\tau_\varepsilon^{(l)}, \tau_{v,j}^{(l)}) \mid Y_{1:K,j}^F, \Theta^{l-1}] \\ &\propto \log(p(\tau_\varepsilon^{(l)} \mid \alpha,\beta)) + \log(p(\tau_{v,j}^{(l)} \mid \alpha,\beta)) + E[\log L_j^{(l)}]. \end{aligned} \quad [S23]$$

We maximize Eq. S23 with respect to $\tau_{v,j}^{(l)}$ and $\tau_\varepsilon^{(l)}$ to obtain

$$\tau_{v,j}^{(l)} = \frac{K+\alpha}{2\sum_{k=1}^{K}\left(W_{k-1|K,j}^{(l)} - \Re\{W_{k,k-1|K,j}^{(l)}\}\right) + W_{K|K,j}^{(l)} + \beta}, \quad [S24]$$

$$\tau_\varepsilon^{(l)} = \frac{\alpha - 1 + JK}{\sum_{k,j}\left((Y_{k,j}^{F,(l)})^2 + W_{k|K,j}^{(l)} - 2\Re\{Y_{k,j}^{F,(l)*}\Delta Z_{k|K,j}^{(l)}\}\right) + \beta}. \quad [S25]$$

respectively. The initial state $\Delta Z_0(\omega_j)$ can be simply estimated using the Fourier transform of original time-series $X_1$ as $\Delta Z_0(\omega_j) = FX_1$. The EM algorithm iterates between E-steps and M-steps until $\|\Delta Z_{k|K}^{(l)} - \Delta Z_{k|K}^{(l-1)}\|^2 / \|\Delta Z_{k|K}^{(l-1)}\|^2 < \epsilon$ where $\epsilon \in (0, 0.001)$ or $l = L_{\max}$, where $L_{\max}$ is a pre-specified number of maximum iterations.

## SI Applications

**A. Examples of Multitaper Spectrogram Analyses.** In formulating our concept of non-stationarity, we assumed minimal intervals on which the time series is stationary. This assumption derives from the common practice by investigators across many fields of science of assuming a minimal interval of stationarity. Table S1 documents several examples. These examples show that the minimal stationary interval is generally chosen to be small relative to the length of the times series.

**B. Time-Domain Signal Extraction.** Because the SS-MT paradigm estimates the increment differences, we use Eq. 14 to extract the slow-delta (Fig. S1*A*), theta (Fig. S1*B*), and alpha oscillations (Fig. S1*C*), and Eq. 15 to estimate instantaneous amplitudes (Fig. S1*C*) for 12 sec of data in Fig. 2*B* beginning at 140 minutes. The magnitudes of the oscillations are consistent with what is seen in the SS-MT spectrograms. The alpha and theta oscillations show substantial slow-delta amplitude modulation consistent with previous reports [32]. Fig. S2 shows the slow-delta (0.1 to 4Hz), the theta (4 to 8 Hz) and the alpha (8 to 12 Hz) oscillations extracted from the EEG time series in Fig. S1 along with their associated 95% credibility intervals.

**C. Denoising and Leakage Reduction Analysis.** We computed the eigenspectrograms (Fig. S3) for the MT spectrogram in Fig. 2*D* and the eigenspectrograms (Fig. S4) for the SS-MT spectrogram for Fig. 2*F*. The eigenspectrograms resemble their respective periodograms. Comparing the eigenspectrograms with the resultant spectrograms shows that averaging contributes significantly to denoising the spectrogram.

Fig. S5*A* (S5*B*) shows state variance estimates and the steady-state Kalman gains for the first tapered series as a function of frequency for the complex Kalman filter algorithms used to compute the SS-MT spectrogram for the simulated time series in Fig. 1*F* (the EEG time series in Fig 2*F*).

**Table S1. Examples of Multitaper Spectrogram Analyses**

| | Article | Application | Stationary Interval<br>Overlap<br>Total Time |
|---|---|---|---|
| 1 | Prechtl et al, PNAS, 1997 (1) | Voltage sensitive dye measurements of electrical activity in the turtle cortex | 1 second<br>Non-overlapping<br>Total length: 8 sec |
| 2 | Llinas et al. PNAS, 1999 (2) | Magnetoencephalographic activity in neurogenic pain, tinnitus, Parkinson's disease and depression | 5 seconds<br>1 seconds overlap<br>Total length: 10 min |
| 3 | Van der Meer and Redish, FINS, 2009 (3) | Relationship of gamma oscillations to different behavioral states in the rodent | 500 msec<br>50 msec overlap<br>Total length: 6 sec |
| 4 | Mhuircheartaigh et al. Science Translational Medicine, 2013 (4) | Electroencephalogram of patients under general anesthesia | 3 seconds<br>0.4 seconds overlap<br>Total length: 116 min |
| 5 | Schmandt et al. Geophysical Research Letters, 2013 (5) | Analysis of seismic and infrasound measurements during control flood experiments | 2 minutes<br>Non-overlapping<br>Total length: 5 days |
| 6 | Williams et al. eLife, 2013 (6) | Electroencephalogram measurements of brain dynamics in patients with severe brain injuries | 2-3 seconds<br>Non-overlapping<br>Total length: 5 hours |
| 7 | Mandelblat-Cerf et al. PLoS One, 2014 (7) | Local field potential for zebra finch song | 9 milliseconds<br>1 millisecond overlap<br>Total length: 500 msec |
| 8 | Takahashi et al. Nature Communications, 2015 (8) | Analysis of large-scale oscillations in neural spiking activity in the non-human primate motor cortex | 250 milliseconds<br>248 millisecond overlap<br>Total length: 500 msec |
| 9 | Purdon et al. Anesthesiology, 2015 (9) | Electroencephalogram studies of patients under general anesthesia | 3 seconds<br>0.5 seconds overlap<br>Total length:20-180 min |
| 10 | Cornelissen et al. eLife, 2015 (10) | Electroencephalogram studies of neonates under general anesthesia | 2 seconds<br>1.9 seconds overlap<br>Total length:76-268 min |
| 11 | Prerau et al. Physiology, 2016 (11) | Electroencephalogram studies of sleep | 2.5 second to 30 sec<br>2.45–25 sec overlap<br>Total length: 8.5 hours |
| 12 | Bhat et al. INTERSPEECH, 2016 (12) | Detecting dysarthric speech | 30 milliseconds<br>20 millisecond overlap<br>Total length: 2-5 sec |
| 13 | Ivory et al. PNAS, 2016 (13) | Studies of biodiversity and variability in Lake Malawi by analyzing long sedentary records | 80K years<br>60K years overlap<br>Total length: 1.2M years |
| 14 | Vlisides et al. Anesthesiology, 2017 (14) | Electroencephalogram of patients under general anesthesia | 3 seconds<br>0.5 seconds overlap<br>Total length: 55 minutes |
| 15 | Hussain et al. SAGEEP, 2017 (15) | Seismic vibrations in Brasilia, Brazil | 1 hour<br>No overlap<br>Total length: 12 days |

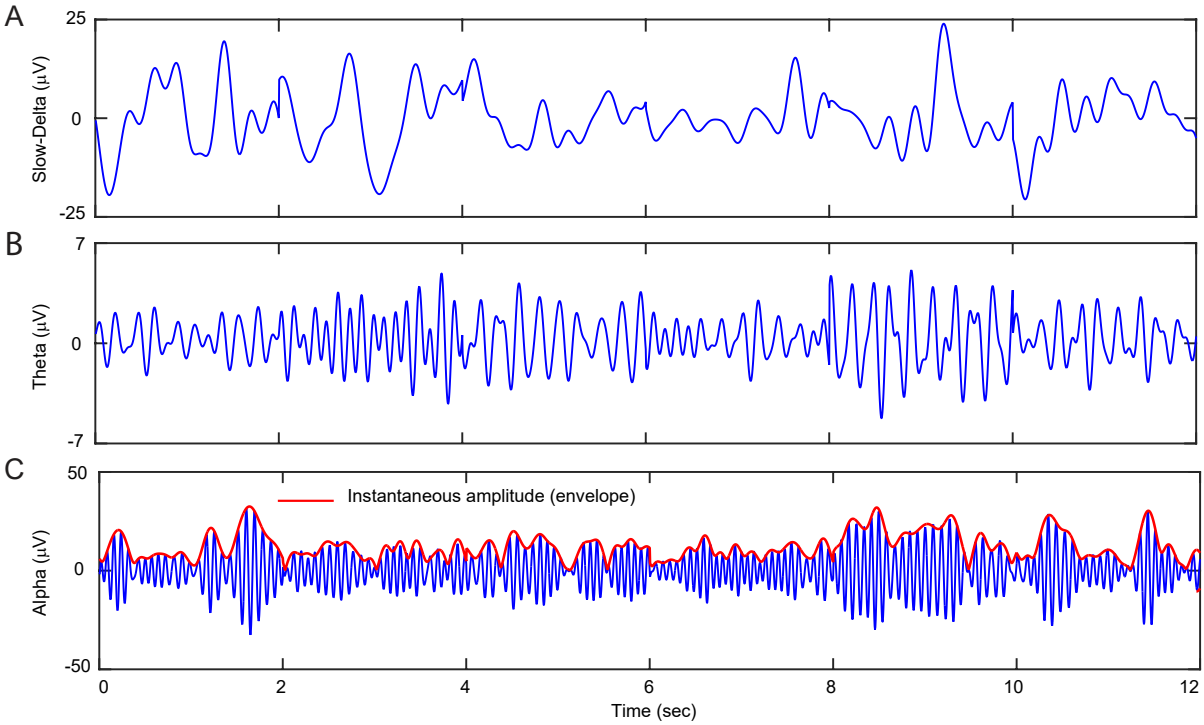


**Fig. S1.** Time-domain signals in different frequency bands extracted from the 12 sec period beginning at 140 minutes for the EEG time series in Fig. 2*B*. (*A*) The slow-delta (0.1 to 4 Hz) oscillation. (*B*) The theta (4 to 8 Hz) oscillation. (*C*) The alpha (8 to 12 Hz) oscillation. The red curve is the instantaneous amplitude.

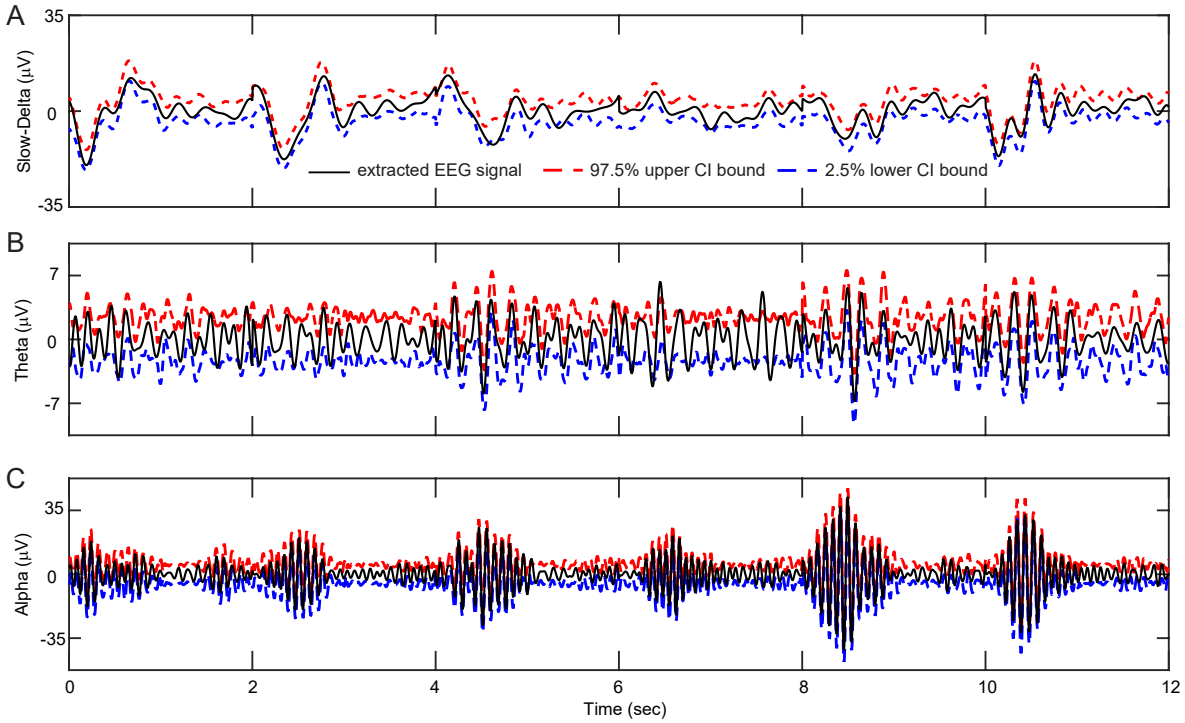


**Fig. S2.** Time-domain signals and their 95% credibility intervals. (*A*) The slow-delta (0.1 to 4Hz) oscillation. (*B*) The theta (4 to 8 Hz) oscillation. (*C*) The alpha (8 to 12 Hz) oscillation. The black curve is the extracted signal, the red dashed curve is the upper bound of the 95% credibility interval, and the blue dashed curve is the lower bound of the 95 % credibility interval.

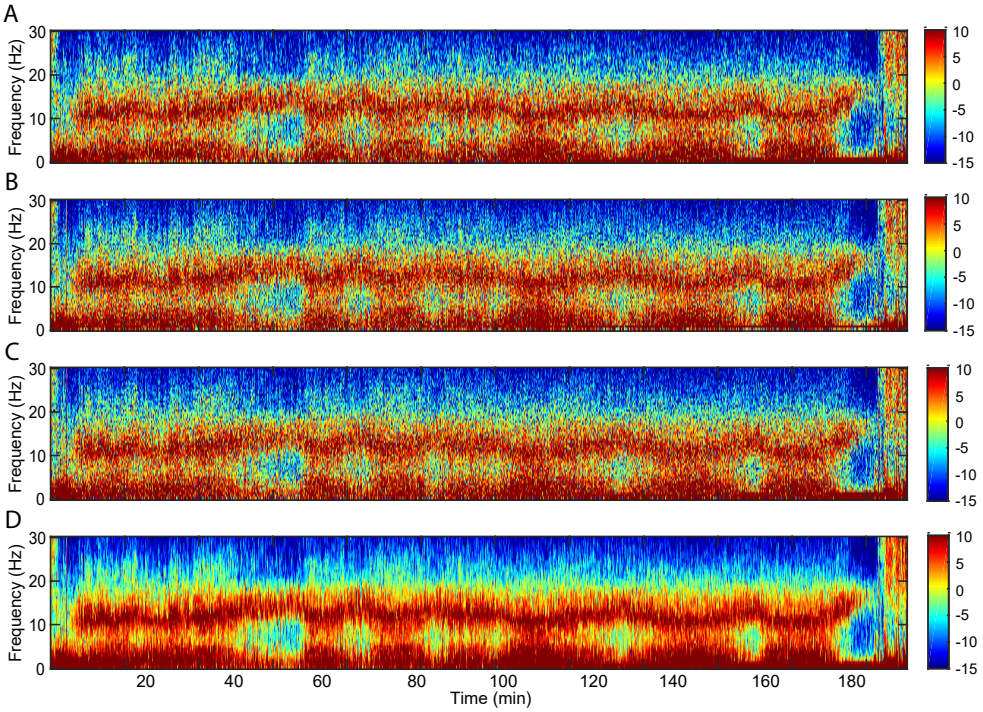


**Fig. S3.** Eigenspectrogram and spectrogram estimates of the multitaper method from EEG data recorded from a patient undergoing sevoflurane-induced general anesthesia (Fig. 2). (*A*)-(*C*) Eigenspectrogram for each tapered signal. (*D*) Multitaper method spectrogram. The color scale is in decibels.

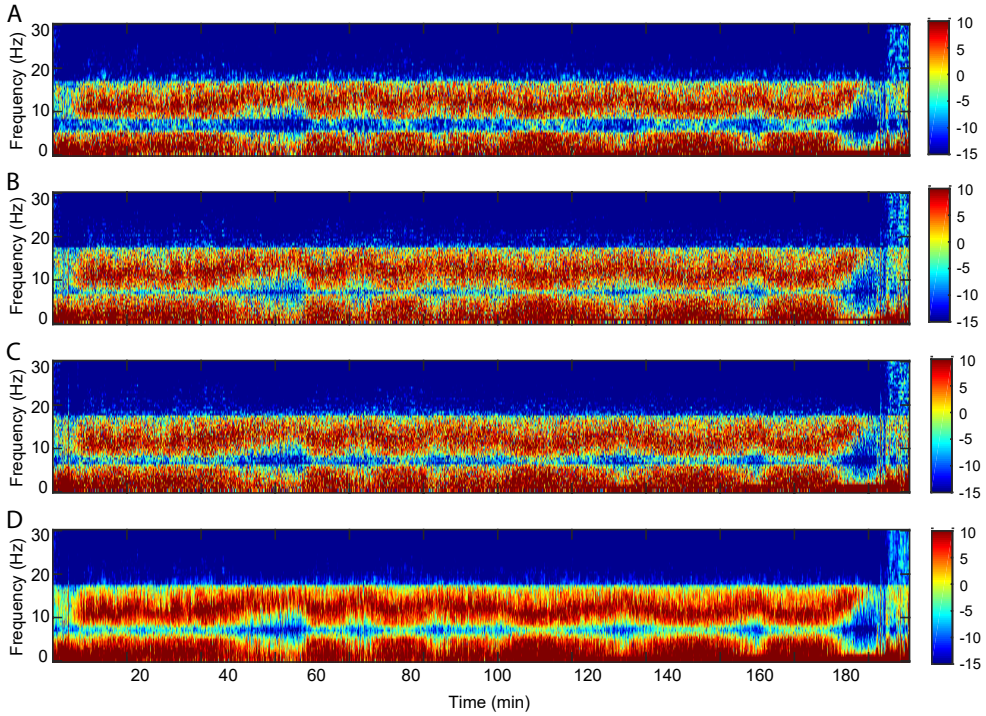


**Fig. S4.** Eigenspectrogram and spectrogram estimates of the state-space multitaper algorithm from EEG data recorded from a patient undergoing sevoflurane-induced general anesthesia (Fig. 2). (*A*)-(*C*) Eigenspectrogram for each tapered signal. (*D*) State-space multitaper spectrogram. The color scale is in decibels.

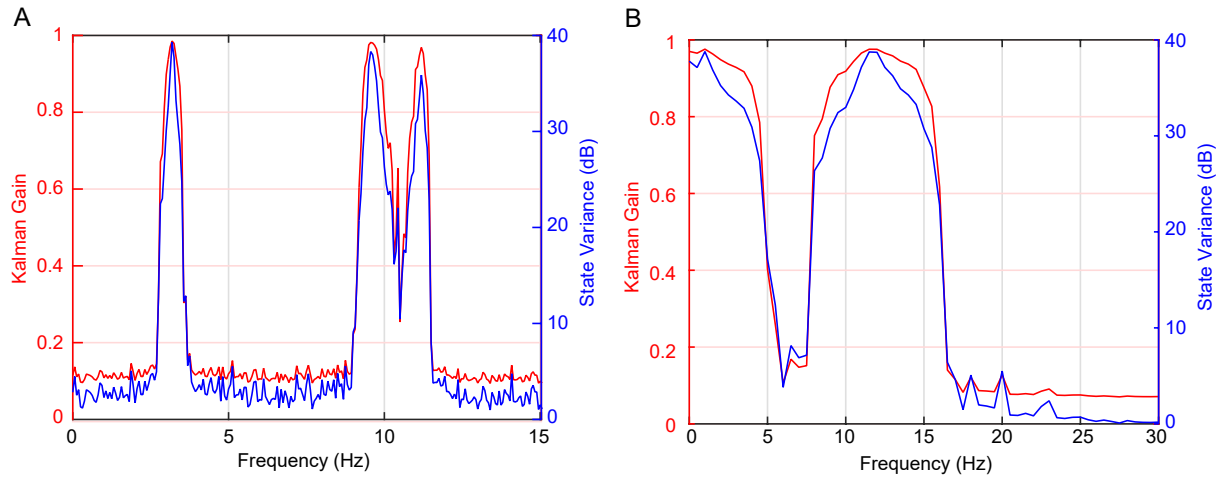


**Fig. S5.** State variance estimates and steady-state Kalman gains for the first tapered time series plotted as a function of frequency for the complex Kalman filter algorithms used to compute the state-space multitaper spectrogram (*A*) for the simulated time series in Fig. 1*F*, (*B*) for the EEG time series in Fig. 2*F*.

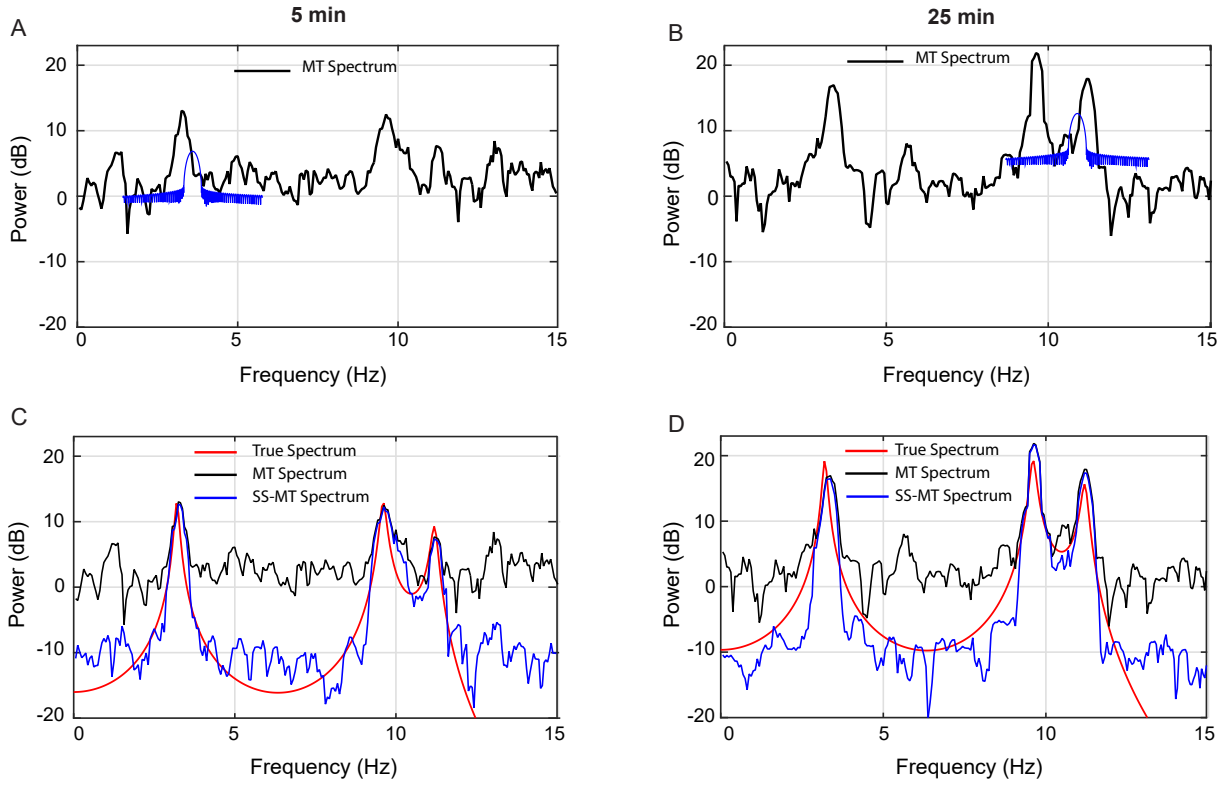


**Fig. S6.** Spectrogram Denoising and Spectral Resolution Analysis. (*A*) MT spectrum (black curve) at 5 minutes (Figs. 1*D* and 1*E*) with power spectral density of the first taper (blue curve) centered at 3.5 Hz to analyze leakage at 4 Hz. The MT spectral resolution was set at 0.5 Hz. (*B*) MT spectrum (black curve) at 25 minutes (Figs. 1*D* and 1*E*) with power spectral density of the first taper (blue curve) centered at 11 Hz. (C) Minute 5 MT spectrum (black curve) from Fig. 1*E*, SS-MT spectrum (blue curve) from Fig. 1*F* and true spectrum (red curve) from Fig. 1*B*. (D) Minute 25 MT spectrum (black curve) from Fig. 1*D*, SS-MT spectrum (blue curve) from Fig. 1*F* and true spectrum (red curve) from Fig. 1*B*.

We analyze the MT and SS-MT spectra for the simulated time series at times 5 and 25 minutes in (Fig. S6). By design, the power spectral density (PSD) of the first taper has a main lobe which is 0.5 Hz in width (blue curve, inset in Figs. S6*A* and S6*B*). The SS-MT spectrum (blue curve in Figs. S6*C* and S6*D*) resembles the true spectrum (red curve, Figs. S6*C* and S6*D*). Figs. S7 and S8 show the PSD of the tapers at minute 25 taken from frequency 9.5 Hz (high signal power) and 6 Hz (low signal power or noise). At 9.5 Hz, the PSDs of the SS-MT tapers (Figs. S7*B*,*D*,*F*) are very similar to that of the MT tapers (Figs. S7*A*,*C*,*E*). The average of the ratios of areas of the main lobes of PSDs for the SS-MT tapers relative to

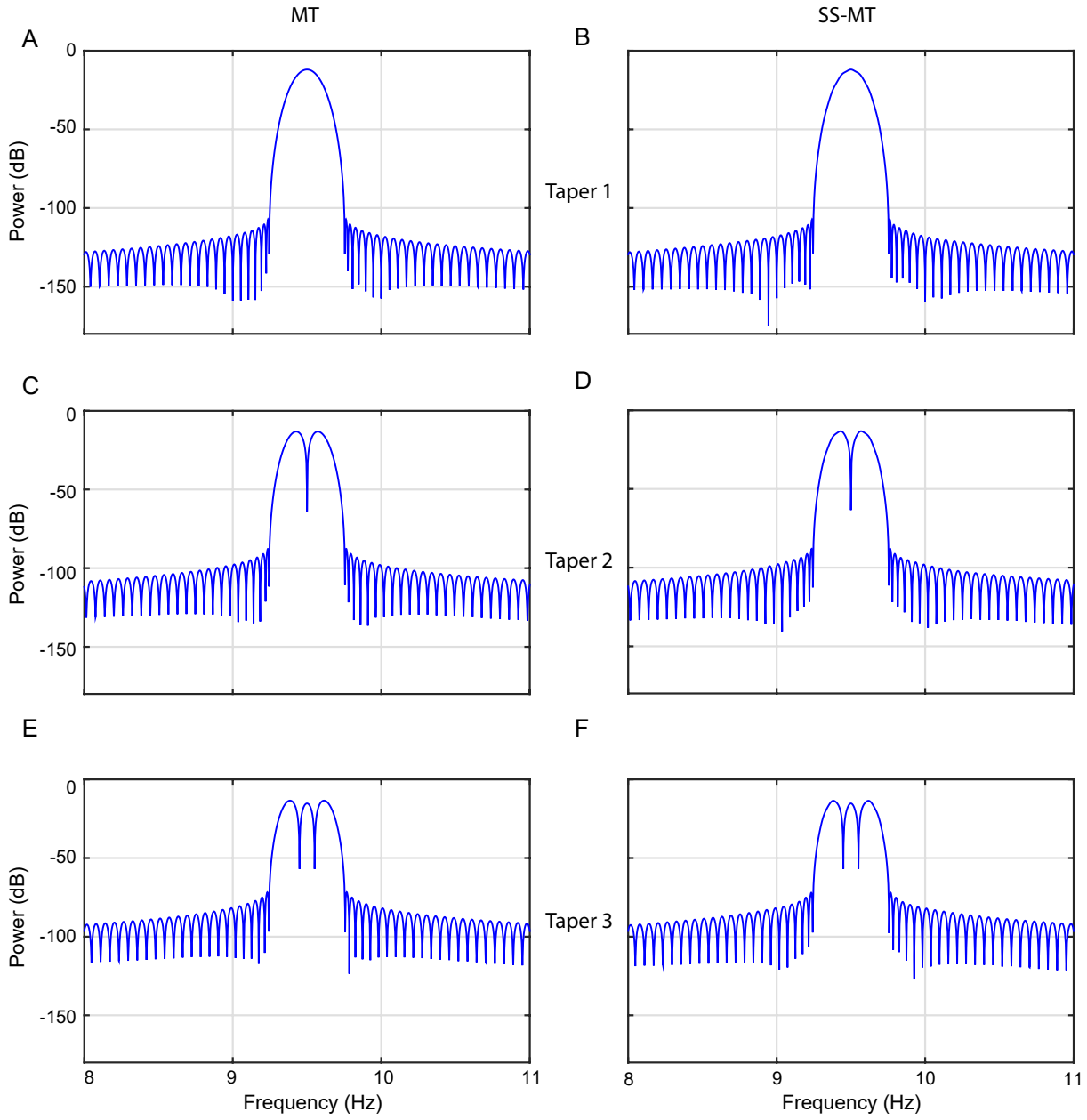


**Fig. S7.** The power spectral density (PSD) of the tapers at 25 minutes and at frequency 9.5 Hz for the MT and the SS-MT spectrograms for the simulated time series in Fig. 1. (*A*), (*C*), and (*E*) show the PSD for MT method for tapers 1, 2, and 3 respectively. (*B*), (*D*), and (*F*) show the PSD for SS-MT algorithm for tapers 1, 2, and 3 respectively.

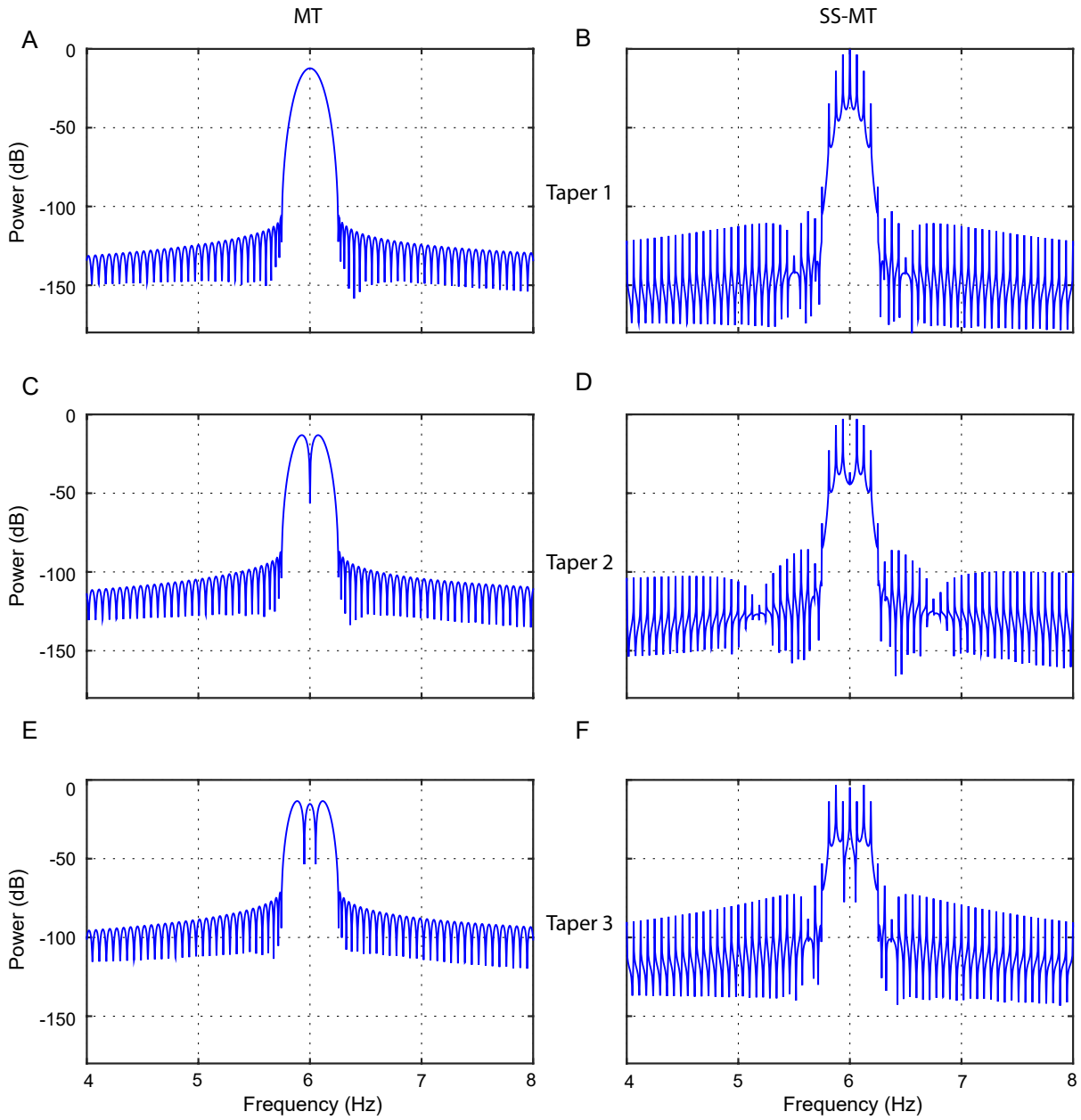


**Fig. S8.** The power spectral density (PSD) of the tapers at 25 minutes and at frequency 6 Hz for the MT and the SS-MT spectrograms for the simulated time series in Fig. 1. (*A*), (*C*), and (*E*) show the PSD for MT method for tapers 1, 2, and 3 respectively. (*B*), (*D*), and (*F*) show the PSD for SS-MT algorithm for tapers 1, 2, and 3 respectively.

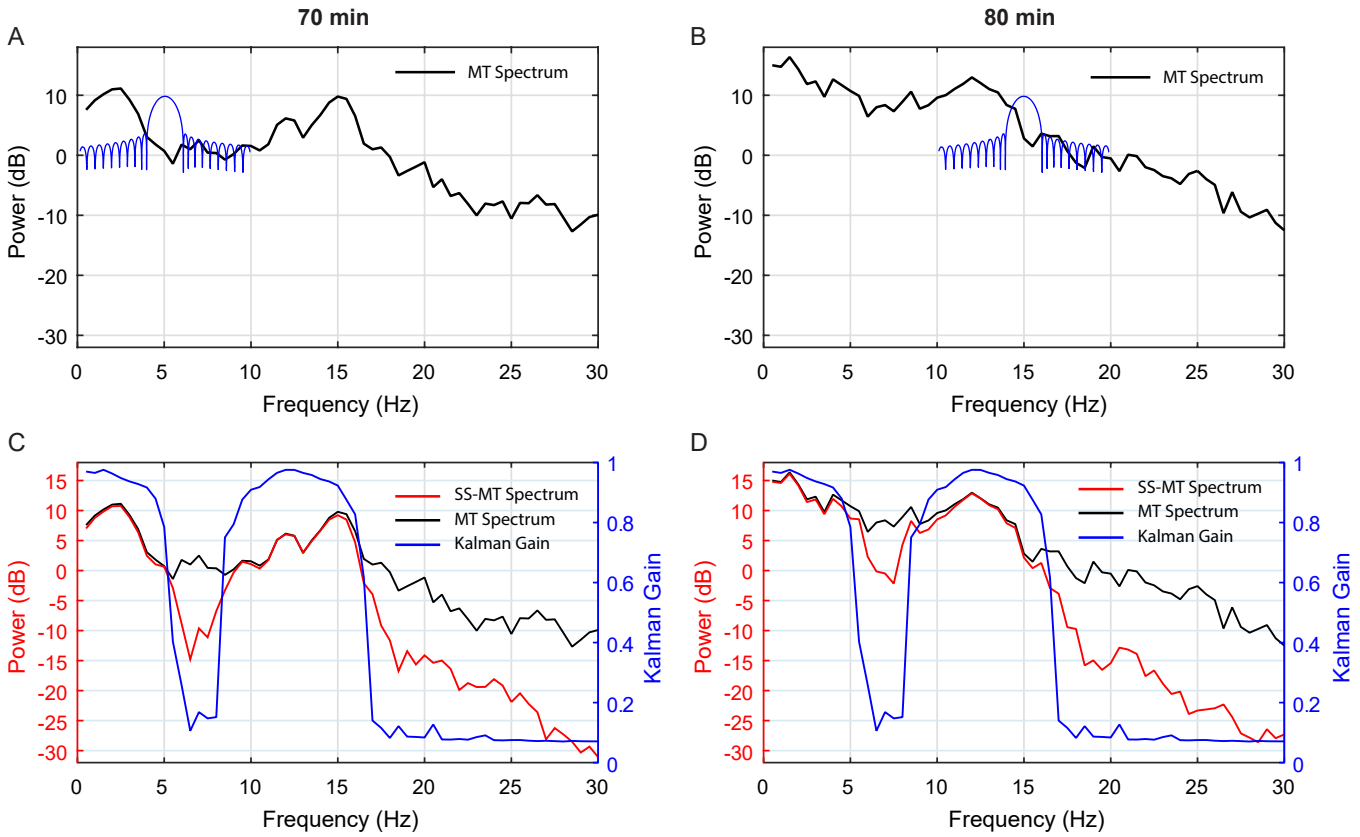


**Fig. S9.** Spectrogram Denoising and Spectral Resolution Analysis. (*A*) MT spectrum (black curve) at 70 minutes (Fig. 2*E*) with power spectral density of the first taper (blue curve) centered at 5 Hz to analyze leakage at 6 Hz. The spectral resolution was set at 2 Hz. (*B*) MT spectrum (black curve) at 80 minutes (Fig. 2*E*) with power spectral density of the first taper (blue curve) centered at 15 Hz. (C) Minute 70 MT spectrum (dashed black curve) from Fig. 2*E*, SS-MT spectrum (red curve) from Fig. 2*F* and SS-MT steady state Kalman gain for first tapered series (red curve). (D) Minute 80 MT spectrum (dashed black curve) from Fig. 2*E*, SS-MT spectrum (red curve) from Fig. 2*F* and SS-MT steady state Kalman gain for first tapered series (blue curve).

the MT tapers is 0.94 and for the corresponding side lobes is 0.95. The PSDs of the SS-MT tapers at 6 Hz (Figs. S8*B*,*D*,*F*) have less area and lower side lobes than the MT PSDs at 6 Hz (Figs. S8*A*,*C*,*E*). Here, the average of the ratios of the areas of the main lobes of PSDs for the SS-MT tapers relative to the MT taper is 0.16 and for the corresponding side lobes is 0.14. The SS-MT algorithm thereby produces effective tapers that appreciable reduce broad band and narrow band leakage from frequencies with low power.

We analyze the MT and SS-MT spectra for EEG time series at times 70 and 80 minutes in Fig. S9. By design, the PSD of the first taper has a main lobe which is 2 Hz in width (blue curve, inset in Figs. S9*A* and S9*B*). Hence, at 70 minutes, the power at 5 Hz is expected to leak into the power at 6 Hz since the difference between 5 and 6 Hz is less than 2 Hz. Similarly, at 80 minutes the power at 15 Hz is expected to leak into the power at 16 Hz (Fig. S9*B*). At minute 70, in the SS-MT spectrum at 6 Hz, the power is 12 dB less than the power in the MT spectrum (Fig. S9*C*). Similarly, at 80 minutes, in the SS-MT spectrum at 16 Hz, the power is 7 dB less than the power in the MT spectrum (Fig. S9*D*). The SS-MT has enhanced denoising and leakage reduction because the Kalman gains at 6 and 16 Hz are approximately 0.1 in both cases (Figs. S9*C* and S9*D*).

For a given set of tapers in the MT analysis, the PSD of the tapers are the same at each frequency (Figs. S7*A*,*C*,*E*, S8*A*,*C*,*E*, S10*A*,*C*,*E*, and S11*A*,*C*,*E*). For the SS-MT analysis the PSD of the tapers depends critically on the Kalman gain. If the Kalman gain is close to 1, then the MT and SS-MT PSD agree (Fig. S7). However, the smaller the Kalman gain the greater the difference between the PSD for the MT and the SS-MT tapers (Figs. S8, S10, and S11). The smaller values of the Kalman gain correspond to frequencies with lower power. Frequencies with low power are unaffected by nearby frequencies with high power because the low Kalman gain places little weight on a new observation which is the potential source of the leakage. The associated PSDs of the SS-MT tapers at frequencies with low power have less area in the main and side lobes than the corresponding MT PSDs. The average of the ratios of the areas of the main lobes of PSDs for the SS-MT tapers relative to the MT taper is 0.17 and for the corresponding side lobes is 0.36 (Fig. S10). The average of the ratios of the areas of the main lobes of PSDs for the SS-MT tapers relative to the MT taper is 0.04 and for the corresponding side lobes is 0.10 (Fig. S11). This property of SS-MT tapers reduces leakage from low power frequencies.

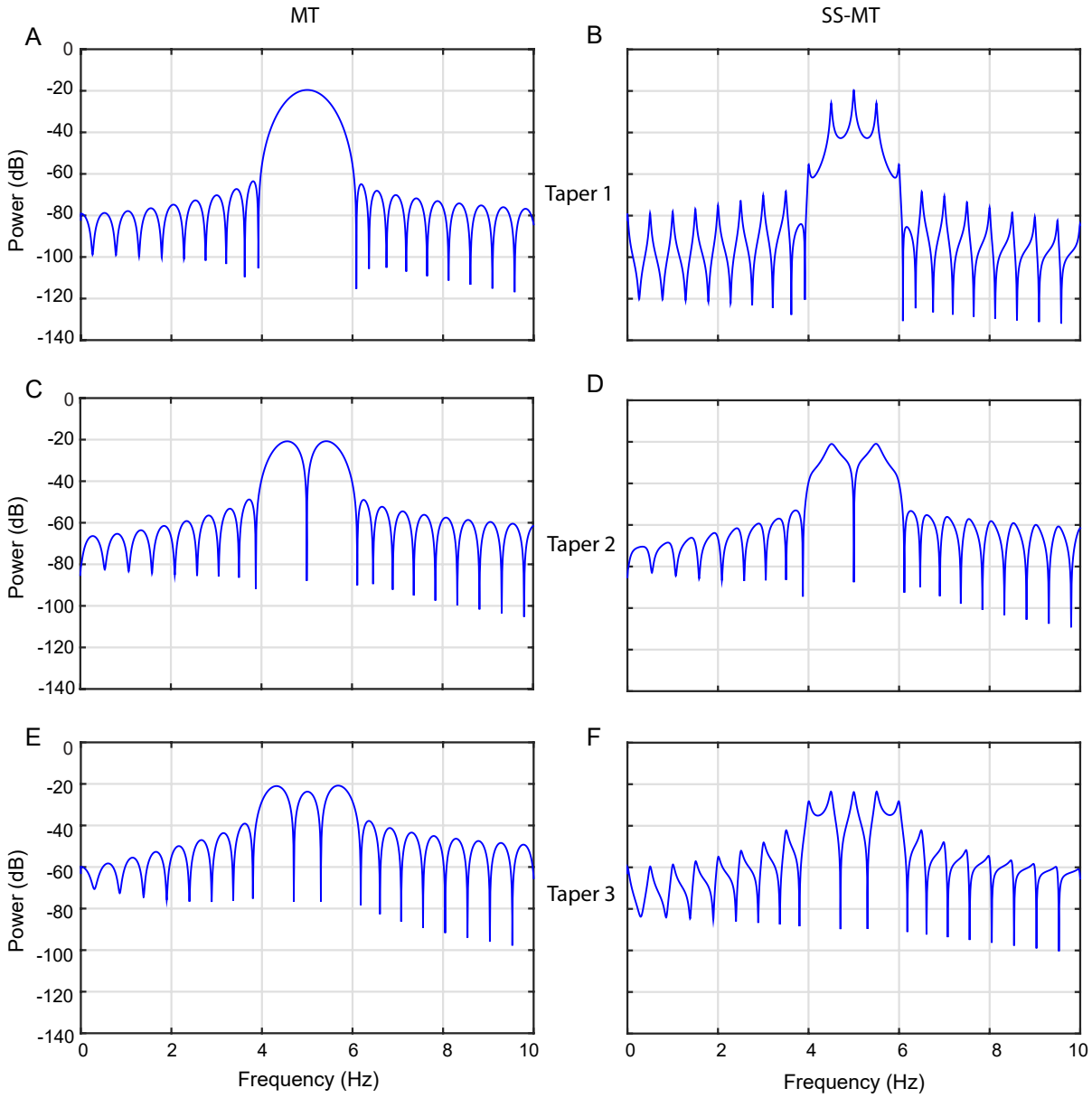


**Fig. S10.** The power spectral density (PSD) of the tapers at minute 70 and at frequency 5 Hz for the MT and the SS-MT spectrograms for the EEG time series in Fig. 2. (*A*), (*C*), and (*E*) show the PSD for MT method for tapers 1, 2, and 3 respectively. (*B*), (*D*), and (*F*) show the PSD for SS-MT algorithm for tapers 1, 2, and 3 respectively.

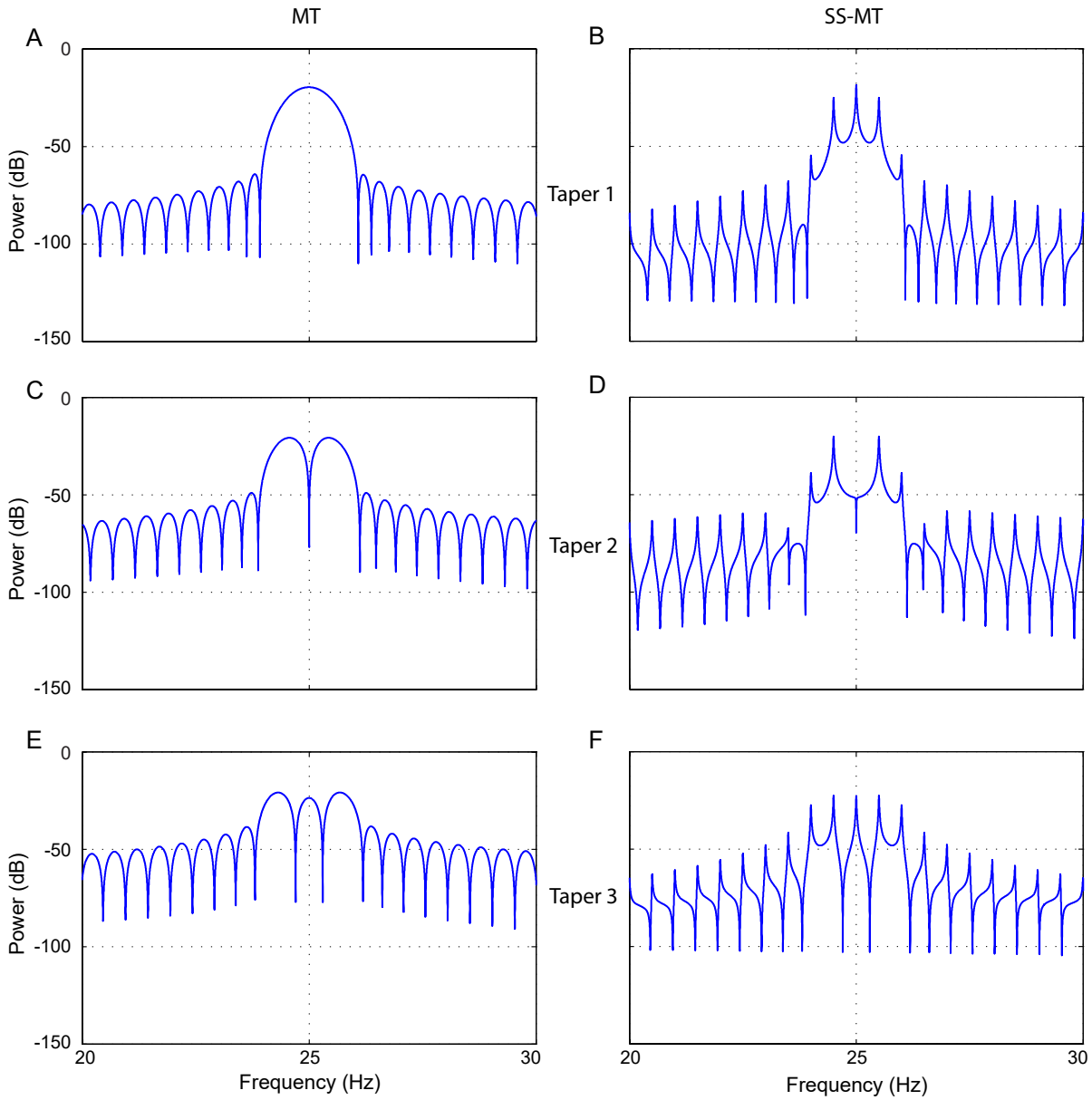


**Fig. S11.** The power spectral density (PSD) of the tapers at minute 80 and at frequency 25 Hz for the MT and the SS-MT spectrograms for the EEG time series in Fig. 2. (*A*), (*C*), and (*E*) show the PSD for MT method for tapers 1, 2, and 3 respectively. (*B*), (*D*), and (*F*) show the PSD for SS-MT algorithm for tapers 1, 2, and 3 respectively.

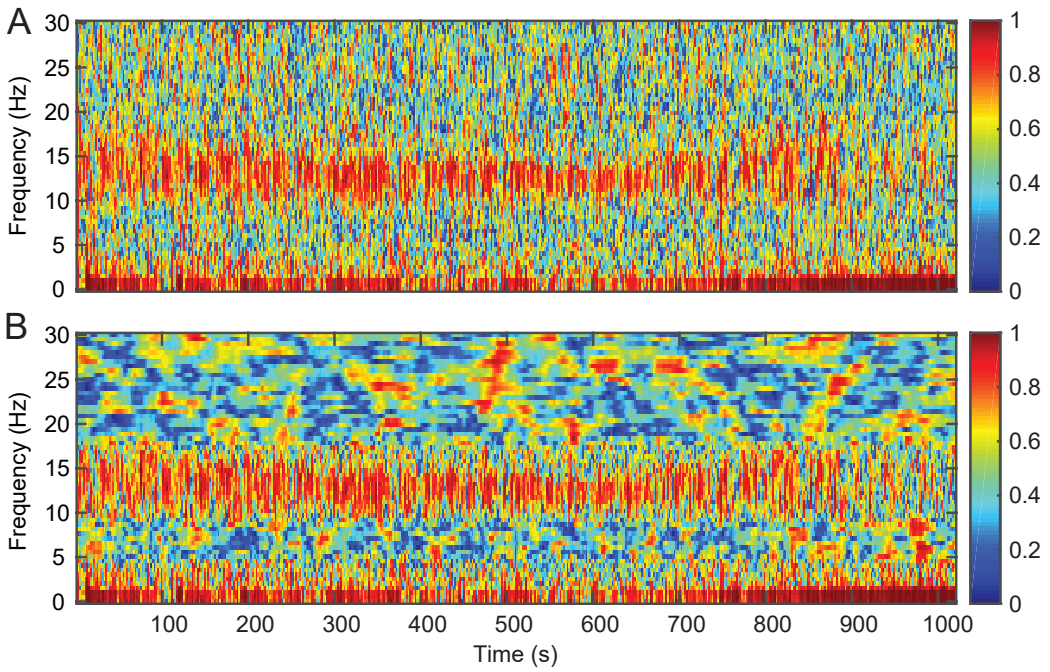


**Fig. S12.** Cross-spectrogram analysis of two EEG time series recorded from a patient under general anesthesia maintained with a propofol infusion. (*A*) Multitaper coherogram. (*B*) State-space multitaper coherogram.

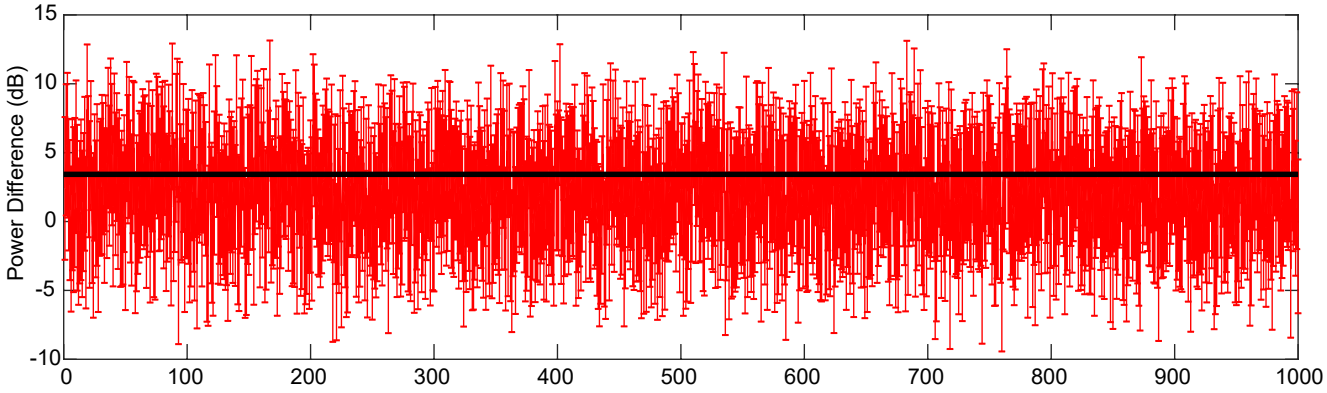


**Fig. S13.** A simulation analysis of the coverage probability for the empirical Bayes 95% confidence intervals. The black horizontal line is 4 dB, the true difference in spectral power at 11.5 Hz between times 27 and 15 minutes. The red vertica lines are the empirical Bayes 95% confidence intervals computed from 1,000 simulated realizations of the AR(6) model in Eq. 18. The simulation estimates the actual frequentist coverage probability to be 0.9660.

**D. Coherence Analysis.** For a coherence analysis, we analyzed 16 minutes of EEG data recorded from a patient receiving general anesthesia maintained by an intravenous propofol infusion. Figure S12 shows the MT coherogram (Fig. S12*A*) and the SS-MT coherogram (Fig. S12*B*). Both methods show high coherence (>0.9) between 10 to 15 Hz during this period that is characteristic of general anesthesia maintained by propofol [32]. The SS-MT coherogram shows greater denoising outside this frequency band than the MT coherogram.

**E. Coverage Probability Analysis.** To assess the accuracy of the empirical Bayes 95% confidence intervals, we conducted a simulation analysis using the non-stationary AR(6) process in Eq. 18. We computed the actual difference in spectral power at 11.5 Hz between times 27 and 15 minutes. We simulated 1,000 time-series from Eq. 18 and fit the SS-MT model to each using the EM algorithm. We used the Monte Carlo algorithm to compute from each SS-MT fit the 95% confidence interval for the spectral power difference by making 3,000 draws from the empirical Bayes posterior distribution $f(\Delta Z|Y,\hat{\Sigma})$, where $\hat{\Sigma}$ denotes the maximum likelihood estimates of the noise floor variance and the state variances at each frequency (see page 4, Inferences for Functions of the Increment Differences). The black horizontal line in Fig. S13 is 4 dB, the true difference in spectral power at 11.5 Hz between times 27 and 15 minutes. The red vertical lines in Fig. S13 are the empirical Bayes 95% confidence intervals computed from 1,000 simulated realizations of the AR(6) model in Eq. 18. The simulation analysis finds that the actual frequentist coverage probability to be 0.966. The lower and upper bounds of the Monte Carlo er-

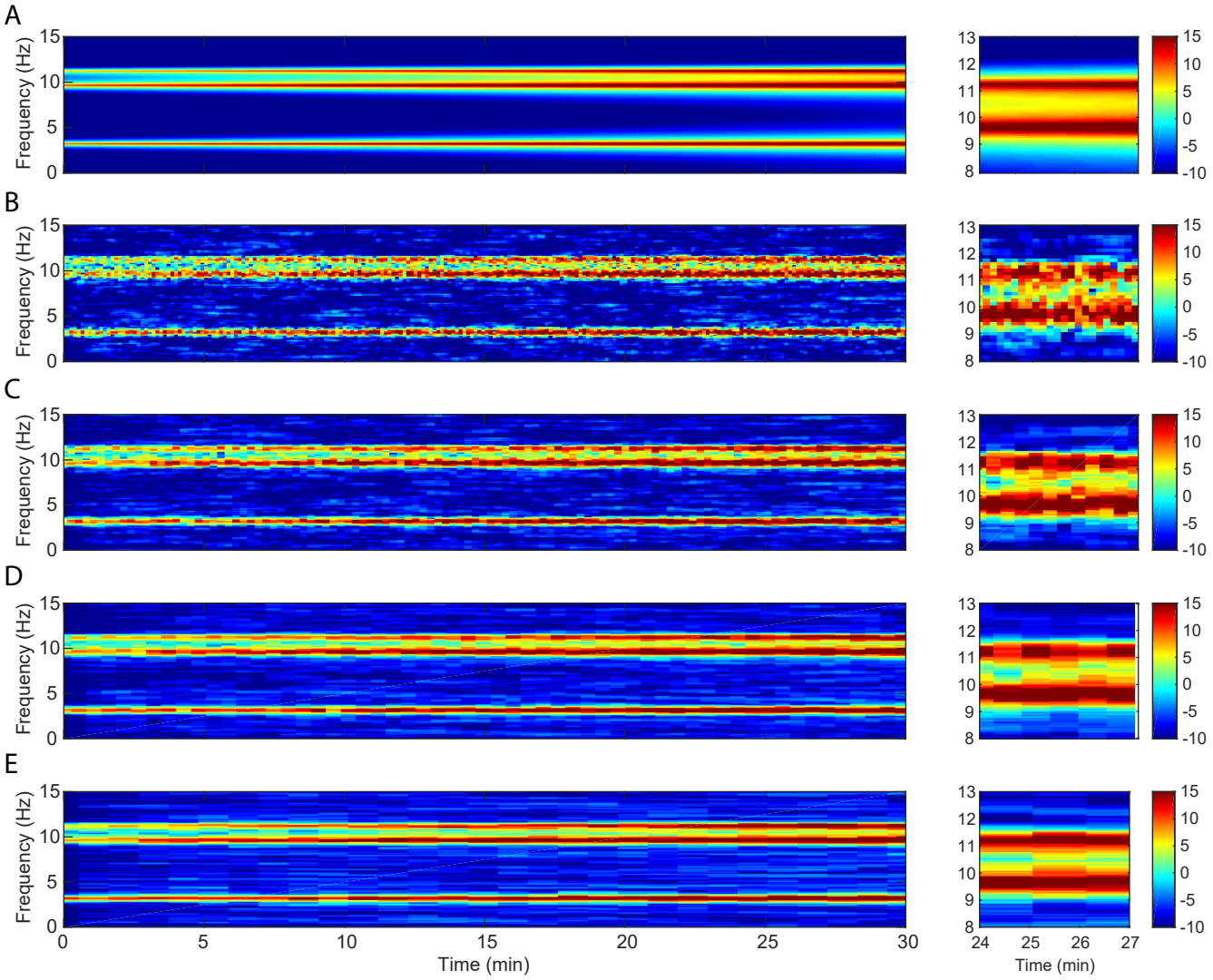


**Fig. S14.** Analysis of the stationary interval choice on spectrogram estimation for the time-varying AR(6) process defined in Eq. 18. (*A*) True spectrogram. (*B*) SS-MT spectrogram estimate for $J = 512$ (8 seconds); (*C*) SS-MT spectrogram estimate for $J = 1,024$ (16 seconds); (*D*) SS-MT spectrogram estimate for $J = 2,048$ (32 seconds); (*E*) SS-MT spectrogram estimate for $J = 4,096$ (64 seconds). The right column shows for each panel a zoomed in display of the three minutes between minutes 24 to 27. The color scale is decibels

ror based on 1,000 draws from a binomial distribution with $p = 0.95$ is [0.947 0.964]. The fact that the actual coverage probability is just beyond the upper Monte Carlo error bound suggests that the SS-MT 95% confidence interval is slightly conservative. This observation is reassuring given that the SS-MT model lies outside the model class that generated the data.

**F. Choice of Stationary Interval Length.** Using the AR (6) model in Eq. 18, we analyzed the effect of stationary interval choice on spectrogram estimation. For this model there is no "ground truth" interval choice because there is no finite interval on which the data are stationary. Moreover, the SS-MT model is outside the model class generating the data. In the analysis in Fig. 1*F* we chose J=1,024, the number of data points per stationary interval. In this analysis of the stationary interval choice we fit the SS-MT model with $J = 512$ (8 seconds) (Fig. S14*B*); $J = 1,024$ (16 seconds) (Fig. S14*C*); $J = 2,048$ (32 seconds) (Fig. S14*D*); and $J = 4,096$ (64 seconds) (Fig. S14*E*).

Table S2 shows for seven frequencies the mean-squared error (MSE) computed by averaging the sum of squared differences between each estimate (periodogram, MT, SS-periodogram, and SS-MT) and the true spectrogram over all time intervals for the four different choices of stationary interval lengths. In Table S2, we report the MSE for 3 frequencies with high power: 3.5 Hz, 9.5 Hz, and 11.5 Hz; 3 frequencies with low power: 1.5 Hz, 6.5 Hz and 12.5 Hz; and one frequency with intermediate pwoer: 10.5 Hz (Fig. S14). For each stationary interval length, the SS-MT spectrogram estimates have the smallest MSEs for all 4 methods.

Within the SS-MT estimates, the stationary interval length that minimizes the MSE differs in relation to the magnitude of the spectral power at a given frequency. For two of the frequencies with high power (9.5 Hz and 11.5 Hz) and the frequency with intermediate power (10.5 Hz), the MSE was minimized by choosing a 64-second stationary interval. The MSE for

**Table S2. Mean-Squared Error as a Function of Stationary Interval Length**

| Frequency (Hz) | Periodogram | MT | SS-P | SS-MT |
|---|---|---|---|---|
| $J = 512$ (8 seconds) | | | | |
| 1.5 | 7 | 7 | -17 | -18 |
| 3.5 | 34 | 29 | 33 | 28 |
| 6.5 | 8 | 7 | -15 | -18 |
| 9.5 | 34 | 34 | 34 | 33 |
| 10.5 | 17 | 12 | 13 | 5 |
| 11.5 | 31 | 26 | 30 | 25 |
| 12.5 | 8 | 6 | -15 | -20 |
| $J = 1,024$ (16 seconds) | | | | |
| 1.5 | 7 | 5 | -16 | -22 |
| 3.5 | 35 | 27 | 34 | 27 |
| 6.5 | 8 | 5 | -15 | -21 |
| 9.5 | 34 | 30 | 33 | 29 |
| 10.5 | 16 | 11 | 10 | 5 |
| 11.5 | 32 | 23 | 32 | 23 |
| 12.5 | 8 | 5 | -17 | -19 |
| $J = 2,048$ (32 seconds) | | | | |
| 1.5 | 7 | 5 | -16 | -22 |
| 3.5 | 35 | 25 | 35 | 25 |
| 6.5 | 8 | 5 | -13 | -18 |
| 9.5 | 33 | 29 | 33 | 29 |
| 10.5 | 16 | 10 | 8 | 2 |
| 11.5 | 34 | 19 | 34 | 19 |
| 12.5 | 6 | 5 | -16 | -18 |
| $J = 4,096$ (64 seconds) | | | | |
| 1.5 | 7 | 5 | -19 | -21 |
| 3.5 | 33 | 26 | 33 | 26 |
| 6.5 | 7 | 4 | -11 | -18 |
| 9.5 | 34 | 28 | 33 | 28 |
| 10.5 | 17 | 10 | 8 | -1 |
| 11.5 | 38 | 17 | 38 | 17 |
| 12.5 | 6 | 4 | -13 | -17 |

The MT and SS-MT spectrograms were estimated using 2 tapers ($J = 512$), 4 tapers ($J = 1.024$), 8 tapers ($J = 2.048$), and 16 tapers ($J = 4,096$) to keep spectral resolution at 0.5 Hz. Table entries are in decibels, i.e., $10 \log_{10}(\text{MSE})$. MT: multitaper spectrogram; SS-P: state-space periodogram; SS-MT: state-space multitaper spectrogram.

the third frequency with high power (3.5 Hz) was minimized by a 32-second stationary interval choice. The spectrogram estimates for the high-power frequencies using the 64-second stationary interval (Fig. S14$E$) resemble most closely the true spectrogram (Fig. S14$A$). For the three frequencies with low power (1.5Hz, 6.5Hz and 12.5Hz) the minimum MSE stationary interval choice was the 16-second interval. Although the 16-second stationary interval spectrogram estimate (Fig. S14$C$) has the smallest MSEs for the low-power frequencies, the differences between it and the other spectrograms at these frequencies is not visibly discernible in Fig. S14.


1. Prechtl JC, Cohen LB, Pesaran B, Mitra PP, Kleinfeld D (1997) Visual stimuli induce waves of electrical activity in turtle cortex. *Proc Natl Acad Sci USA* 94(14):7621–7626.
2. Llinás RR, Ribary U, Jeanmonod D, Kronberg E, Mitra PP (1999) Thalamocortical dysrhythmia: A neurological and neuropsychiatric syndrome characterized by magnetoencephalography. *Proc Natl Acad of Sci USA* 96(26):15222–15227.
3. van der Meer MA, Redish AD (2009) Low and high gamma oscillations in rat ventral striatum have distinct relationships to behavior, reward, and spiking activity on a learned spatial decision task. *Front Integr Neurosci* 3:9.
4. Ní Mhuircheartaigh R, Warnaby C, Rogers R, Jbabdi S,Tracey I (2013) Slow-wave activity saturation and thalamocortical isolation during propofol anesthesia in humans. *Sci Transl Med* 5(208):208ra148.
5. Schmandt B, Aster RC, Scherler D, Tsai VC, Karlstrom K (2013) Multiple fluvial processes detected by riverside seismic and infrasound monitoring of a controlled flood in the Grand Canyon. *Geophysical Research Letters* 40(18):4858–4863.
6. Williams ST, et al. (2013) Common resting brain dynamics indicate a possible mechanism underlying zolpidem response in severe brain injury. *eLife* 2:e01157.
7. Mandelblat-Cerf Y, Fee MS (2014) An automated procedure for evaluating song imitation. *PLoS One* 9(5):e96484.
8. Takahashi K, et al. (2015) Large-scale spatiotemporal spike patterning consistent with wave propagation in motor cortex. *Nat Commun* 6:7169.
9. Purdon PL, Sampson A, Pavone KJ, Brown EN (2015) Clinical electroencephalography for anesthesiologists: Part I: background and basic signatures. *Anesthesiology* 123(4):937–960.
10. Cornelissen L, Kim SE, Purdon PL, Brown EN, Berde CB (2015) Age-dependent electroencephalogram (EEG) patterns during sevoflurane general anesthesia in infants. *eLife* 4:e06513.
11. Prerau MJ, Brown RE, Bianchi MT, Ellenbogen JM, Purdon PL (2017) Sleep neurophysiological dynamics through the lens of multitaper spectral analysis. *Physiology* 32(1):60–92.
12. Bhat C, Vachhani B, Kopparapu SK (2016) Recognition of dysarthric speech using voice parameters for speaker adaptation and multi-taper spectral sstimation. *INTERSPEECH*.
13. Ivory SJ, et al. (2016) Environmental change explains cichlid adaptive radiation at Lake Malawi over the past 1.2 million years. *Proc Natl Acad Sci USA* 113(42):11895–11900.
14. Vlisides PE, et al. (2017) Neurophysiologic correlates of ketamine sedation and anesthesia: a high-density electroencephalography study in healthy volunteers. *Anesthesiology* 127(1):58–69
15. Hussain Y, et al. (2017) Spectral analysis of the recorded ambient vibration at a mass movement in Brasilia. *Symposium on the Application of Geophysics to Engineering and Environmental Problems* 214–218.